Ferroelectric-enhanced Z-schematic electron transfer in BiVO₄-BiFeO₃-CuInS₂ for efficient photocatalytic pollutant degradation

Houfen Li, Xie Quan*, Shuo Chen, Hongtao Yu

Key Laboratory of Industrial Ecology and Environmental Engineering (Ministry of Education), School of Environmental Science and Technology, Dalian University of Technology, Dalian, 116024, China

ABSTRACT

The unique charge carrier migration with electrons transferring from photocatalytic oxidation system to photocatalytic reduction system in Z-scheme system is the key step which ensures their high reduction and oxidation capacities. However, it is difficult to control this vectorial electron transfer as it could only be realized with the downward band bending from photocatalytic oxidation system (PS II) to photocatalytic reduction system (PS I) at the interface. For ferroelectric materials, different band bending can be formed due to the switched polarization-induced electric fields inside the materials, and the required band bending can be obtained using suitable poling conditions. Therefore, Z-schematic charge carrier transfer should be enhanced by inserting a ferroelectric material with downward band bending between PS II and PS I. Herein, this inference was verified by the improved photocurrent density and generated reactive oxygen species on BiVO₄-BiFeO₃-CuInS₂+ with the polarization-induced electric field oriented from CuInS₂ to BiVO₄. Finally, the photocatalytic degradation rate of 4-nitrophenol on BiVO₄-BiFeO₃-CuInS₂ was proved to be 2.8 and 16.9 times higher than those on CuInS₂ and BiVO₄-CuInS₂, respectively, and the degradation rate of 2,4-dichlorophenol on the former was 1.6 and 3.4 times those on the latter, demonstrating the polarization-induced electric field led to improved photocatalytic performance.

© 2017 Elsevier B.V. All rights reserved.

1. Introduction

Photocatalysis is a promising technology to solve environmental pollution issues by oxidizing and reducing pollutants using only solar light as the energy source [1,2]. However, the practical application of this technology is hindered by the low efficiency of photocatalysts. To address this issue, composite photocatalysts are commonly used to expand the available light spectra by means of sensitization [3], surface modification [4–6], or to enhance charge carrier separation with the aid of a built-in electric field [7]. Nevertheless, electrons and holes in composite materials migrate to and accumulate in less negative conduction bands and less positive valence bands, respectively, weakening the oxidation and reduction abilities of charge carriers compared with single-component photocatalysts. The Z-scheme system, which is generally composed of two photocatalysts and an electron mediator, seems an effective approach to overcome these drawbacks. This type of photocatalytic system proceeds through a two-photon excitation process mimicking photosynthesis [8–11]. Electrons photogenerated within the photocatalytic oxidation system (PS II) transfer to the surface of photocatalytic reduction system (PS I) via an electron mediator and recombine with the holes of the latter, while holes with high oxidation ability in PS II, as well as electrons with high reduction ability in PS I, are preserved. The unique advantages of Z-scheme photocatalytic system result in its superiority for the degradation of refractory organic pollutants [2,12], water splitting [13–16], and other applications. However, very limited success in the construction of Z-scheme systems has been achieved, as it is difficult to control the vectorial electron transfer from PS II to PS I in such systems.

The charge carrier transfer of Z-scheme system was originally realized via ionic redox shuttles in solution [17–19], under conditions in which back-reactions easily occurred and photocatalyst recovery was difficult. Recently, Z-scheme systems with solid electron mediators [10,20,21], or even those realized by interparticle Z-schematic electron migration between PS I and PS II without electron mediators [22,23], were reported to avoid the problems caused by ionic electron shuttles. For the all-solid Z-scheme systems, the energy band alignments play an important role because the charge carrier transfer at the interface is affected by the energy band bend-

---

* Corresponding author.
  E-mail address: quanxie@dlut.edu.cn (X. Quan).

ing of semiconductors and electron mediators [24,25]. Therefore, it is essential to adjust the energy band structures of PS I and PS II in order to obtain Z-schematic electron migration. Electric fields, such as external electric fields [26], and electric fields induced by polarization [27], have a significant impact on the energy band structure of semiconductors. Recent work has demonstrated that the polarization-induced electric field inside ferroelectric materials can cause energy band bending with intensity reaching several hundred meV. For example, band bending with values of 0.3–0.5 V and 0.3–0.8 V were reported for $BaTiO_3$ and $LiNbO_3$, respectively [28,29]. This intensity is of similar magnitude to that of p-n junctions, which allows the energy band bending to be a powerful driving force of charge carrier transfer in the materials [30,31]. Moreover, the internal electric field's intensity and its orientation can be changed under different polarization conditions, which implied that the upward (downward) energy band bending can be achieved with a suitable poling direction [32,33]. As the vectorial electron transfer in the Z-scheme system is realized through downward band bending from PS II to PS I, the Z-schematic charge carrier transfer should be enhanced by inserting a ferroelectric material with this type of band bending between PS II and PS I.

Monoclinic bismuth vanadate (m-$BiVO_4$) is a visible-light responsive photocatalyst with a bandgap of ~2.4 eV and is a promising candidate for PS II of Z-scheme system due to the high oxidation capacity of its photogenerated holes within the valence band [34,35]. The ternary sulfide-$CuInS_2$, with relatively high conduction band, is an attractive candidate for PS I due to the high reduction capacity of electrons under light irradiation. Moreover, the latter could absorb long-wavelength light efficiently attributed to its narrow band gap (~1.5 eV), and its energy band structure matches with that of $BiVO_4$ [36,37]. Therefore, taking $BiVO_4$ and $CuInS_2$ as PS II and PS I, respectively, by inserting the ferroelectric material $BiFeO_3$ between PS II and PS I, the effect of the polarization-induced electric field on Z-schematic charge carrier transfer was investigated. Due to the relative energy band locations of these materials, the interfacial energy band bending of the semiconductors and the energy band structures of $BiVO_4$-$BiFeO_3$-$CuInS_2$ after electron transfer balance were represented in Scheme 1a. In this case, the electrons generated on $BiVO_4$ and $BiFeO_3$ cannot transfer to the conduction band of $CuInS_2$ due to the high energy barrier between the conduction bands of $BiFeO_3$ and $CuInS_2$. In addition, it is difficult to transfer to the valence band of $CuInS_2$ because of the wide band gap between the conduction band of $BiFeO_3$ and the valence band of $CuInS_2$. However, after an internal electric field oriented from $CuInS_2$ to $BiVO_4$ was formed by poling $BiFeO_3$ (Scheme 1b), the photogenerated electrons on the conduction band of $BiFeO_3$ could transfer via the Z-schematic mechanism to the valence band of $CuInS_2$ under the driving of the electric field and recombine with the photogenerated holes in $CuInS_2$, which indicated that more photogenerated electrons in $CuInS_2$ could be retained. In contrast, with the electric field in $BiFeO_3$ oriented from $BiVO_4$ to $CuInS_2$ (Scheme 1c), photogenerated holes, instead of electrons, were expected to migrate from $BiFeO_3$ to $CuInS_2$, which would greatly decrease the number of electrons in $CuInS_2$. Therefore, the $BiVO_4$-$BiFeO_3$-$CuInS_2$ system with an electric field from $CuInS_2$ to $BiVO_4$ was anticipated to possess higher reduction and oxidation capacities originating from the Z-scheme mechanism.

2. Experimental section

2.1. Preparation of $BiVO_4$-$BiFeO_3$-$CuInS_2$ photocatalysts

$BiVO_4$-$BiFeO_3$-$CuInS_2$ was prepared by depositing $BiVO_4$, $BiFeO_3$, and $CuInS_2$ in sequence. First, $BiVO_4$ was deposited on an FTO glass substrate by chemical solution deposition. The precur-

sor solution of $BiVO_4$ (0.2 M) was prepared according to a reported method [39], and it was spin-coated on the substrate at 1200 rpm, followed by drying at 300 °C for 5 min and rapid annealing at 500 °C for 5 min. Second, using a similar process, 0.2 M $BiFeO_3$ precursor solution was prepared, and was spin-coated on the as-prepared $BiVO_4$ film [39,40]. Afterwards, the sample was dried at 300 °C for 5 min and was rapidly annealed at 550 °C for 5 min. To adjust the thickness of $BiFeO_3$, the spin speeds were controlled at 300 rpm, 450 rpm, 600 rpm, and 1200 rpm, respectively. Finally, $BiVO_4$-$BiFeO_3$-$CuInS_2$ was prepared by depositing $CuInS_2$ on the $BiVO_4$-$BiFeO_3$ sample. $CuInS_2$ was fabricated using a solvothermal process [41], typically, 0.023 M $CuCl_2 \cdot 2H_2O$, 0.023 M $InNO_3 \cdot 5H_2O$, 0.104 M $CS(NH_2)_2$, 0.045 M $C_2H_2O_4 \cdot 2H_2O$ and 0.227 mmol CTAB were dissolved and dispersed in 40 mL of ethanol, which was transferred into a stainless steel autoclave and reacted at 200 °C for 12 h. The dark brown product was rinsed with de-ionized water and ethanol, and was subsequently dried in vacuum. To deposit $CuInS_2$ on the $BiVO_4$-$BiFeO_3$ sample, 10 mg of $CuInS_2$ was dispersed uniformly in 20 mL of isopropanol, and the $BiVO_4$-$BiFeO_3$ sample was placed in the solution. After evaporating the solvent at 80 °C, $BiVO_4$-$BiFeO_3$-$CuInS_2$ was obtained.

To polarize $BiVO_4$-$BiFeO_3$-$CuInS_2$, the sample was connected to the anode (cathode) of a power supply and was poled at 100 V for 30 min using FTO glass as the counter electrode in air [42].

2.2. Characterization

The morphology of $BiVO_4$, $BiFeO_3$, $CuInS_2$, and $BiVO_4$-$BiFeO_3$-$CuInS_2$ was observed using an S-4800 field emission scanning electron microscope (SEM, Hitachi Co., Japan). In addition, the element maps of $BiVO_4$-$BiFeO_3$-$CuInS_2$ were scanned using energy dispersive X-ray spectroscopy (EDS, 550i, IXRF Systems, Japan). The crystal structures of the samples were characterized using an X-ray diffractometer (XRD, EMPYREAN, PANalytical, Netherlands). The valence band-Fermi level energy band gaps (E_{vf}) of the materials were analyzed by an X-ray photoelectron spectrometer (XPS, ESCALAB 250XI, Thermo Fisher Scientific, USA) with Al Kα X-ray irradiation (1486.6 eV). The ultraviolet-visible diffuse reflectance spectra (DRS) of $CuInS_2$, $BiVO_4$-$CuInS_2$, and $BiVO_4$-$BiFeO_3$-$CuInS_2$ were recorded on a Shimadzu UV-2450 spectrophotometer. The photocurrent densities and the Mott-Schottky plots were measured in Na_2SO_4 electrolyte (0.1 M) on an electrochemical station (CHI660D, Shanghai Chenhua Instrument Co., China). Superoxide radicals ($\bullet O_2^-$) and hydroxyl radicals ($\bullet OH$) were trapped with 5,5-dimethyl-L-pyrroline-n-oxide (DMPO, 50 mM) in aqueous solution and methanol solution, respectively, and were detected using an electron spin resonance (ESR) spectrometer (A200, Bruker, Germany).

2.3. Photocatalytic reactions

The photocatalytic degradation of 4-nitrophenol (4-NP) and 2,4-dichlorophenol (2,4-DCP) on $BiVO_4$-$BiFeO_3$-$CuInS_2$ was performed to evaluate the photocatalytic capability of the photocatalyst. A high-pressure xenon short arc lamp (CHF-XM35-500W, Beijing Changtuo Co.) was used as the light source, with a visible light cut-off filter (≥420 nm). The light intensity was adjusted to 100 mW cm^{-2} using a digital radiometer (FZ-A, Photoelectric Instrument Factory, Beijing Normal University). To avoid accumulation of holes inside the material during the photocatalytic process, $BiVO_4$-$BiFeO_3$-$CuInS_2$ (effective area of 3 cm^2) was connected to a Pt electrode via an electrochemical station, and they were placed vertically into 20 mL of 4-nitrophenol or 2,4-dichlorophenol solution (5 mg L^{-1}). No electrolyte was added, and the bias was set to 0 vs NHE. Before the photocatalytic process, the solution was stirred in the dark for 30 min to ensure adsorption equilibrium. The pol-
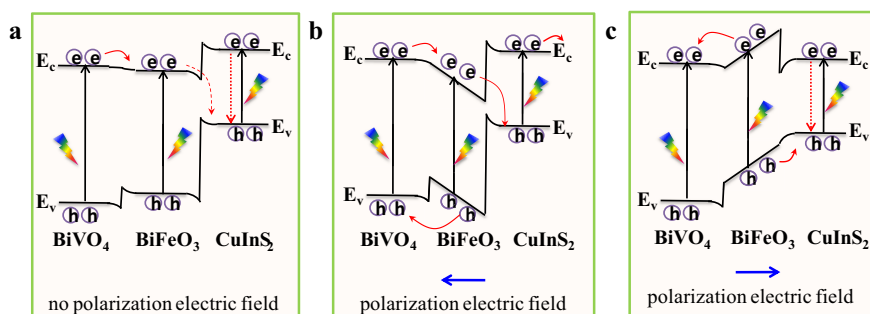
Scheme 1. Charge carrier transfer behaviors in BiVO$_4$-BiFeO$_3$-CuInS$_2$: (a) without polarization; (b), (c) after polarization with different poling directions.
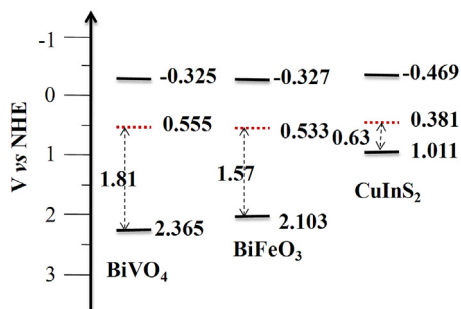

Fig. 1. Relative energy band levels of BiVO$_4$, BiFeO$_3$ and CuInS$_2$.

lutant concentration was determined by high-performance liquid chromatography (HPLC) with a UV detector (Waters 2695, Photodiode Array Detector 2996). The variation in the total organic carbon (TOC) concentration after 2,4-dichlorophenol degradation was analyzed using a TOC analyzer (multi N/C2100, Analytik Jena AG).

3. Results and discussion

3.1. Energy band structures of BiVO$_4$, BiFeO$_3$ and CuInS$_2$ photocatalysts

First, the energy band structures of BiVO$_4$, BiFeO$_3$ and CuInS$_2$ were confirmed to verify the predicted charge carrier behavior. The Fermi energy levels (E$_f$), the valence band-Fermi level energy

gaps (E$_{vf}$) [38], and the energy band gaps of BiVO$_4$, BiFeO$_3$, and CuInS$_2$ were determined using Mott-Schottky plots, valence band X-ray photoelectron spectroscopy and ultraviolet-visible diffuse reflectance spectra, respectively, with results shown in Figs. S1–S3. Accordingly, the energy band alignments of the three semiconductors are schematically illustrated in Fig. 1. These energy band structures indicated the energy band bending of BiVO$_4$-BiFeO$_3$-CuInS$_2$ was in accord with the inference in Scheme 1a.

3.2. Structure, crystal phase and light absorption properties of BiVO$_4$-BiFeO$_3$-CuInS$_2$

The structure of BiVO$_4$-BiFeO$_3$-CuInS$_2$ was investigated based on its cross-sectional SEM image and corresponding element maps. Result in Fig. 2 disclosed that the "BiVO$_4$-BiFeO$_3$-CuInS$_2$" structure was successfully obtained after depositing BiVO$_4$, BiFeO$_3$, and CuInS$_2$ on the FTO substrate layer by layer. This structure endowed the BiFeO$_3$ interlayer a key role in the charge carrier transfer between BiVO$_4$ and CuInS$_2$, and was essential to study the effect of the internal electric field of BiFeO$_3$. The thickness of each layer was estimated from the cross-sectional SEM images of BiVO$_4$, BiFeO$_3$, and CuInS$_2$ in Fig. S4 as 100 nm, 70 nm, and 1000 nm, respectively. Additionally, the HRTEM image of BiVO$_4$-BiFeO$_3$-CuInS$_2$ in Fig. S5 exhibited the lattice spacings of BiVO$_4$, BiFeO$_3$ and CuInS$_2$ are 0.310 nm, 0.281 nm, and 0.320 nm, respectively, demonstrating the well growth of different materials. And the lattice changes at the interfaces of BiVO$_4$-BiFeO$_3$ and BiFeO$_3$-CuInS$_2$ further proved the formation of "BiVO$_4$-BiFeO$_3$-CuInS$_2$" structure. The crystal phases of the materials were determined by
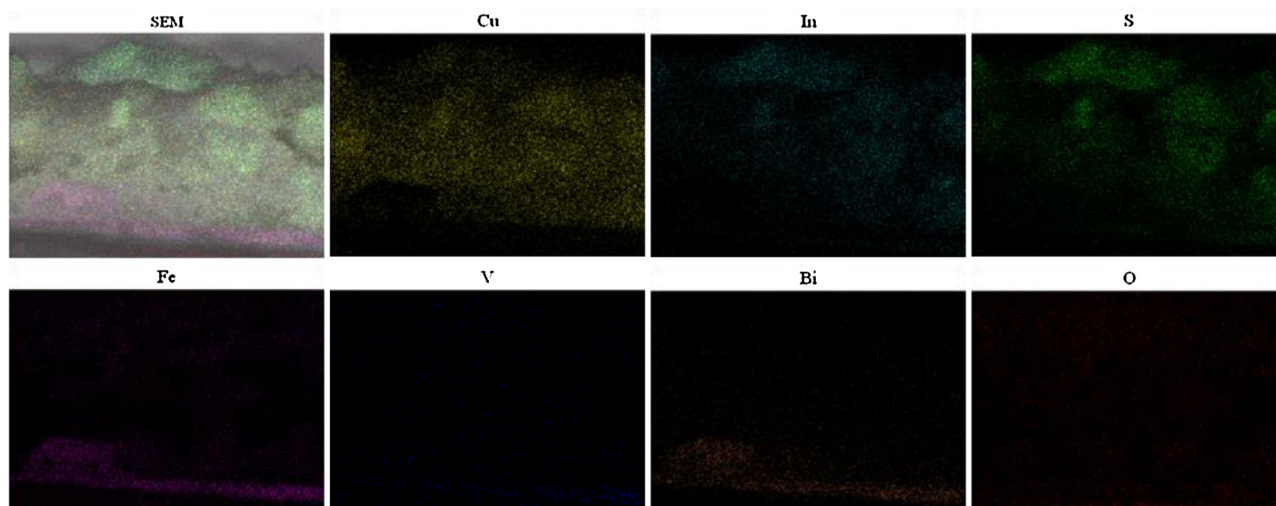

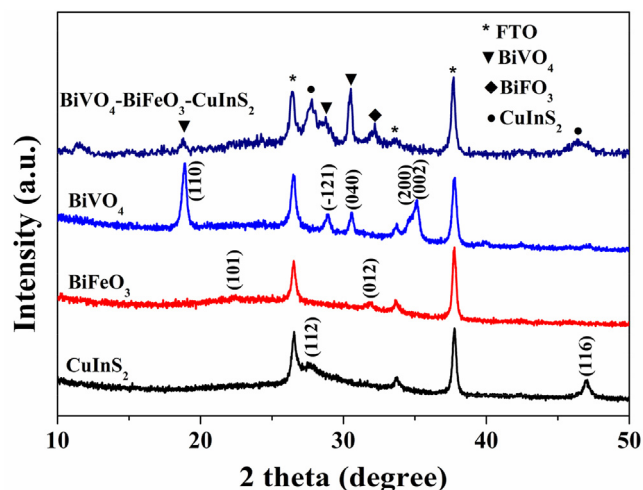**Fig. 2.** Cross-sectional SEM image and the element maps of BiVO$_4$-BiFeO$_3$-CuInS$_2$.

Fig. 3. XRD patterns of $BiVO_4$, $BiFeO_3$, $CuInS_2$, and $BiVO_4$-$BiFeO_3$-$CuInS_2$.

Fig. 4. DRS of FTO, $BiVO_4$, $BiVO_4$-$CuInS_2$ and $BiVO_4$-$BiFeO_3$-$CuInS_2$.

Fig. 5. Photocurrent density-time plots of $BiVO_4$-$BiFeO_3$-$CuInS_2$ under visible light irradiation (experimental conditions: 0 V vs NHE, 0.1 M Na_2SO_4, $\lambda \geq 420$ nm).

$CuInS_2$, including PS II and PS I, could be excited under visible light irradiation in the following experiment ($\lambda \geq 420$ nm).

3.3. Study of the charge carrier transfer mechanism of $BiVO_4$-$BiFeO_3$-$CuInS_2$

To ascertain the effect of polarization-induced electric field on the charge carrier transfer behavior, $BiVO_4$-$BiFeO_3$-$CuInS_2$ was poled under different conditions, and the electron transfer behavior was studied with the photocurrent density tests. The results are shown in Fig. 5. As can be seen, the visible light photocurrent density of $CuInS_2$ was -0.07 mA cm^{-2} at 0 V vs NHE, however, the value decreased to -0.005 mA cm^{-2} and -0.01 mA cm^{-2} when $BiVO_4$-$CuInS_2$ and $BiVO_4$-$BiFeO_3$-$CuInS_2$, respectively, were used. This change occurred because the photogenerated electrons in $BiVO_4$ and $BiFeO_3$ were hindered by the energy band barrier between $BiFeO_3$ and $CuInS_2$ and were unable to migrate to the conduction band of $CuInS_2$. Additionally, the photogenerated holes in $CuInS_2$ could not transfer to the valence band of $BiFeO_3$, which accelerated the recombination of photogenerated charge carriers within $CuInS_2$. After the material was poled as the anode ($BiVO_4$-$BiFeO_3$-$CuInS_2$+ in Fig. 5) and formed the polarization-induced electric field in Scheme 1b, the photocurrent density of $BiVO_4$-$BiFeO_3$-$CuInS_2$ was improved to -0.15 mA cm^{-2}, which was twice that of pure $CuInS_2$. This remarkably increased photocurrent intensity of $BiVO_4$-$BiFeO_3$-$CuInS_2$+ was a result of electron transfer from the conduction band of $BiFeO_3$ to the valence band of $CuInS_2$ under the driving of polarization-induced electric field, which finally recombine with the photogenerated holes in $CuInS_2$. Consequently, a larger amount of photogenerated electrons in the $CuInS_2$ layer was retained and accumulated in $BiVO_4$-$BiFeO_3$-$CuInS_2$+ than that without polarization and pure $CuInS_2$. The above charge carrier behavior ensured that more photogenerated electrons transferred from $BiVO_4$-$BiFeO_3$-$CuInS_2$+ to the solution, which contributed to the increased photocurrent density. By contrast, when the reverse electric field was formed in $BiFeO_3$, as shown in Scheme 1c ($BiVO_4$-$BiFeO_3$-$CuInS_2$- in Fig. 5), the photogenerated holes, rather than electrons, were driven from $BiFeO_3$ to $CuInS_2$, which was contrary to the direction of the photocurrent inside $CuInS_2$. Therefore, the photogenerated electrons in $CuInS_2$ were prone to be recombined by the holes from $BiFeO_3$ and the photocurrent of $BiVO_4$-$BiFeO_3$-$CuInS_2$- decreased significantly. These photocurrent test results proved that the polarization-induced electric field played a crucial role in regulating the charge carrier transfer, and an appropriate electric field direction could promote electron transfer via the Z-schematic mechanism.

To further demonstrate the charge carrier transfer mechanism of the materials, the reduction and oxidation properties of $BiVO_4$-$BiFeO_3$-$CuInS_2$ composites were determined by detecting

XRD characterization. As shown in Fig. 3, the XRD pattern of $BiVO_4$-$BiFeO_3$-$CuInS_2$ simultaneously exhibited obvious peaks assigned to monoclinic $BiVO_4$ (2θ at $18.67°$, $28.82°$ ($28.95°$), and $30.55°$), hexagonal $BiFeO_3$ ($2\theta = 31.81°$), and cubic $CuInS_2$ ($2\theta = 27.86°$ and $2\theta = 48.38°$). The agreement of the XRD pattern of $BiVO_4$-$BiFeO_3$-$CuInS_2$ with those of $BiVO_4$, $BiFeO_3$, and $CuInS_2$ indicated that the crystal phases and crystallinity of each material were not affected during the preparation process.

As the energy band gap of $BiVO_4$ is the largest of the three materials, followed by $BiFeO_3$ and $CuInS_2$, respectively, each semiconductor would be excited only if the incident light was from the $BiVO_4$ side. Therefore, the optical absorption properties of the as-prepared $CuInS_2$, $BiVO_4$-$CuInS_2$, and $BiVO_4$-$BiFeO_3$-$CuInS_2$ materials were studied by irradiating from the back side of FTO, and the results are shown in Fig. 4. As seen from the figure, with light irradiated from the FTO side, a characteristic absorption peak of FTO material with $\lambda \leq 350$ nm was observed in the spectrum of each sample. For $CuInS_2$, it showed strong absorption in the spectral region with $\lambda \leq 850$ nm due to its narrow energy band gap. In comparison, $BiVO_4$-$CuInS_2$ exhibited enhanced light absorption in the spectral range with $\lambda \leq 500$ nm, which indicated the composite incorporated the light absorption features of $BiVO_4$ and $CuInS_2$. Furthermore, $BiVO_4$-$BiFeO_3$-$CuInS_2$ showed the absorption characteristics of $BiVO_4$, $BiFeO_3$, and $CuInS_2$ simultaneously, with obvious absorption band edges at wavelengths of 500 nm, 550 nm and 850 nm. This result suggested that the materials in $BiVO_4$-$BiFeO_3$-
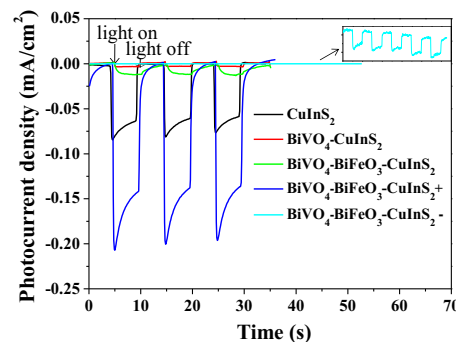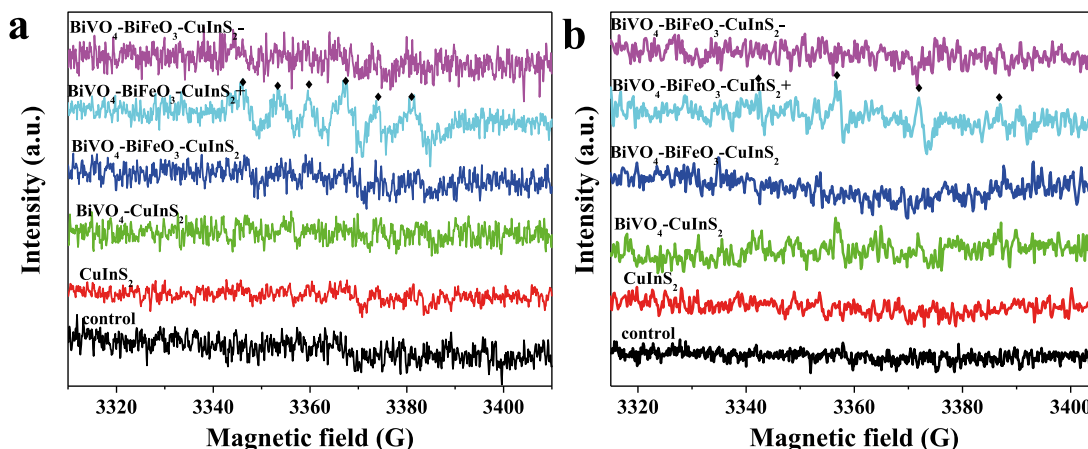
Fig. 6. ESR signals of DMPO-•O_2^- and DMPO-•OH adducts after 25 min irradiation in the presence of different photocatalysts ($\lambda \geq 420$ nm).
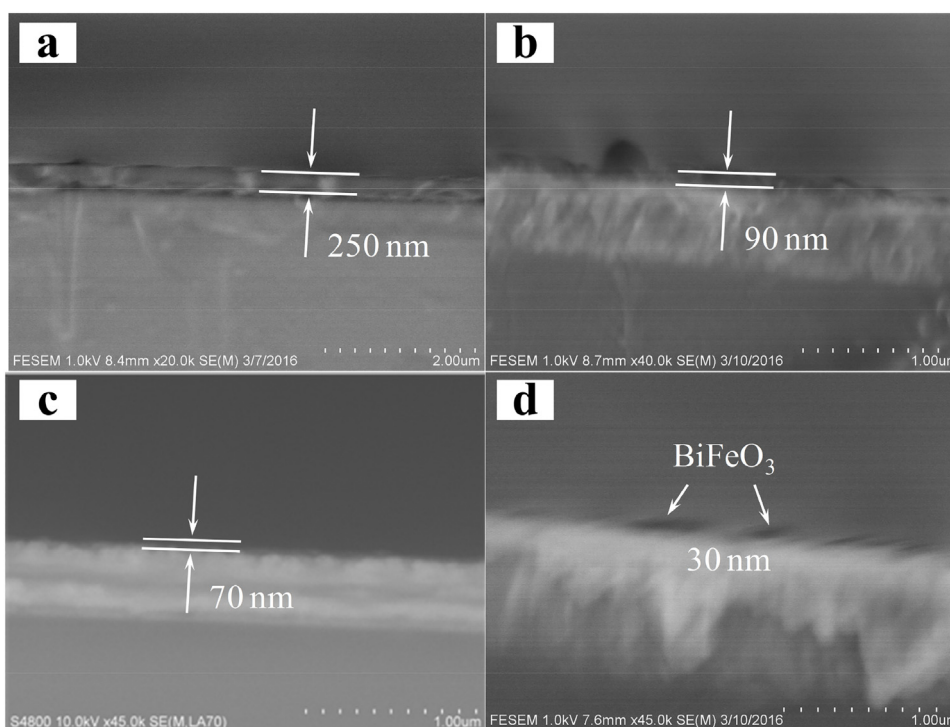

Fig. 7. Thickness of $BiFeO_3$ with different spin speeds: (a) 300 rpm; (b) 450 rpm; (c) 600 rpm; (d) 1200 rpm.

the generation of •O_2^- and •OH under visible light irradiation. As the $CuInS_2$ layer in $BiVO_4$-$BiFeO_3$-$CuInS_2$ was the material directly in contact with the solutions, the generation of reactive oxygen radicals depended on the behavior of the charge carriers on $CuInS_2$. According to the energy band alignments in Scheme 1, the electrons on conduction band of $CuInS_2$ are sufficiently negative to reduce O_2 into •O_2^- in solution (E^o (O_2/•O_2^-) = −0.046 V vs NHE[43]). However, the ESR results in Fig. 6a show that the signal of the DMPO-•O_2^- adduct was very weak in the presence of $CuInS_2$ photocatalyst, indicating that little •O_2^- was produced in this system, due to the high charge carrier recombination rate in $CuInS_2$. It is worth noting that the signal of DMPO-•O_2^- adduct was enhanced when $CuInS_2$ was replaced with the poled $BiVO_4$-$BiFeO_3$-$CuInS_2$+ [44], while the characteristic peaks were not observed when using $BiVO_4$-$CuInS_2$, $BiVO_4$-$BiFeO_3$-$CuInS_2$, or $BiVO_4$-$BiFeO_3$-$CuInS_2$- photocatalysts. In agreement with the result of the photocurrent test, the enhanced •O_2^- generation on

$BiVO_4$-$BiFeO_3$-$CuInS_2$+ confirmed that more photogenerated electrons with high reduction capacity accumulated on the conduction band of $CuInS_2$ under light irradiation, indicative of the important function of the suitable internal electric field in the charge carrier behavior of the materials. Moreover, a similar result was obtained in the •OH test, as shown in Fig. 6b. It depicted no •OH was produced in the solution containing $CuInS_2$, $BiVO_4$-$CuInS_2$, $BiVO_4$-$BiFeO_3$-$CuInS_2$ or $BiVO_4$-$BiFeO_3$-$CuInS_2$- due to the weak oxidation capacity of the holes photogenerated within $CuInS_2$. In contrast, in the presence of $BiVO_4$-$BiFeO_3$-$CuInS_2$+, four peaks with spectral line intensities of 1:2:2:1 were observed at g = 2.0058 [45,46], which revealed that some •OH was generated on this material. The small amount of •OH was produced from •O_2^- because the valence bands of $BiVO_4$, $BiFeO_3$, and $CuInS_2$ were not sufficiently positive for •OH generation (E^o (•OH/H_2O) = 2.38 V vs NHE [43]). The production of reactive oxide species in the presence of $BiVO_4$-$BiFeO_3$-$CuInS_2$+ suggested that high reduction
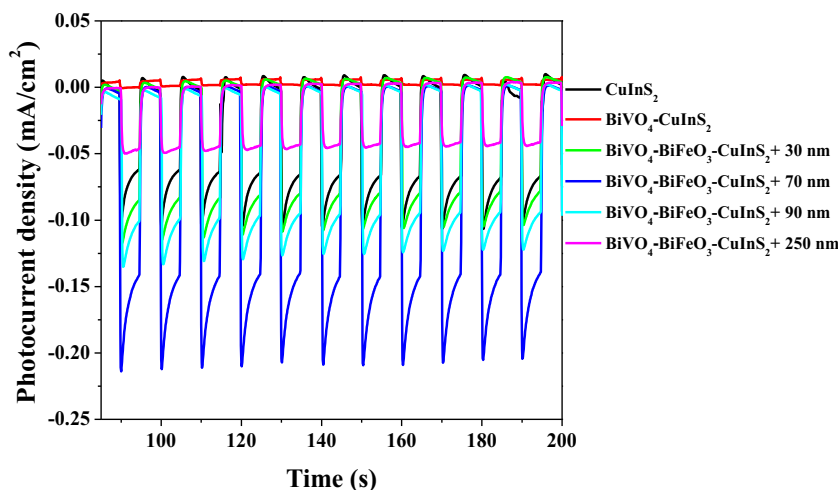
Fig. 8. Photocurrent density-time plots of $BiVO_4$-$BiFeO_3$-$CuInS_2$+ with different $BiFeO_3$ thickness under visible light irradiation (experimental condition: 0 V vs NHE, 0.1 M Na_2SO_4, $\lambda \geq 420$ nm).

and oxidation capacities were expected for $BiVO_4$-$BiFeO_3$-$CuInS_2$+, originating from the Z-scheme mechanism.

3.4. Study of the effect of the $BiFeO_3$ thickness on the properties of $BiVO_4$-$BiFeO_3$-$CuInS_2$

To achieve optimal charge carrier transfer properties, the effect of the thickness of the polarization-induced electric field on the charge carrier migration properties was studied. First, the thickness of the $BiFeO_3$ layer was adjusted between 0 and 250 nm by controlling the spin speed. As shown in Fig. 7, $BiFeO_3$ layers with thicknesses of 250 nm, 90 nm, 70 nm, and 30 nm were obtained at spin speeds of 300 rpm, 450 rpm, 600 rpm, and 1200 rpm, respectively. The photocurrent densities of $BiVO_4$-$BiFeO_3$-$CuInS_2$+ with different $BiFeO_3$ thickness were tested, with results shown in Fig. 8. The photocurrent densities of $BiVO_4$-$BiFeO_3$-$CuInS_2$+ were -0.08 mA cm^{-2} and -0.15 mA cm^{-2} when the thickness of the $BiFeO_3$ interlayer was 30 nm and 70 nm, respectively. The inferior photocurrent intensity of the former may be attributed to the non-continuity of $BiFeO_3$ layer, which led to presence of $BiVO_4$-$CuInS_2$ structure. By contrast, for the 70 nm of $BiFeO_3$ layer, a continuous layer was formed and a uniform electric field was generated in the $BiFeO_3$ layer after polarization. As a result, the directional migration of charge carriers in $BiVO_4$-$BiFeO_3$-$CuInS_2$+ was promoted. By further increasing the thickness of the $BiFeO_3$ layer to 90 nm and 250 nm, respectively, the photocurrent densities of $BiVO_4$-$BiFeO_3$-$CuInS_2$+ was decreased to -0.10 mA cm^{-2} and -0.05 mA cm^{-2}, because that the saturated electric field was more difficult to reach for a thicker $BiFeO_3$ layer, which weakened its promotion of charge carrier migration.

3.5. Study of the photocatalytic performance of $BiVO_4$-$BiFeO_3$-$CuInS_2$ systems

The photocatalytic performance of $BiVO_4$-$BiFeO_3$-$CuInS_2$ materials was evaluated by photocatalytic degradation of 4-nitrophenol (4-NP) and 2,4-dichlorophenol (2,4-DCP), which are representative organic contaminants in water and are among the top priority pollutants.

The photocatalytic degradation plots of 4-NP in Fig. S6 showed that the concentration of 4-NP exhibited almost no change in the absence of photocatalyst, indicating that it was stable under visible light irradiation. The degradation rate constant of 4-NP on $CuInS_2$ was 0.43 h^{-1} as shown in Fig. 9. And the kinetic constants of 4-NP degradation on $BiVO_4$-$CuInS_2$ and $BiVO_4$-$BiFeO_3$-$CuInS_2$ were
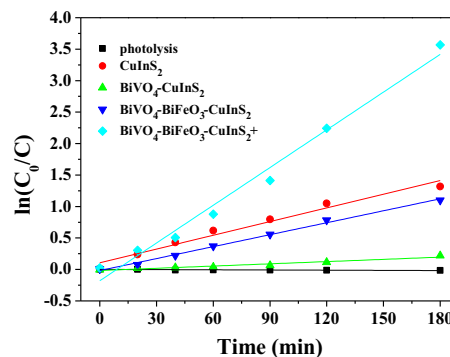

Fig. 9. Degradation kinetics of 4-nitrophenol during the photocatalytic process on different photocatalysts (0 V vs NHE, $\lambda \geq 420$ nm).

0.07 h^{-1} and 0.38 h^{-1}, respectively. The decreased kinetic rates of the heterojunctions were a result of the increased charge carrier recombination at the interface, which was caused by the energy band barriers between $BiVO_4$, $BiFeO_3$ and $CuInS_2$. However, after the ferroelectric layer was poled, the degradation rate constant of 4-NP on $BiVO_4$-$BiFeO_3$-$CuInS_2$+ was improved to 1.19 h^{-1}, which was 2.8 and 16.9 times higher than those on $CuInS_2$ and $BiVO_4$-$CuInS_2$, respectively. This result demonstrated the polarization-induced electric field at the interface was necessary to improve the photocatalytic performance of $BiVO_4$-$BiFeO_3$-$CuInS_2$+ since it functioned as the driving force for Z-schematic charge carrier migration.

To determine the mechanism of 4-NP degradation, the intermediate products of the photocatalytic process were analyzed, and the result are shown in Fig. 10. The substance at 7.4 min was 4-NP, and its concentration decreased as the photocatalytic reaction proceeded. In addition, two products with detection times of 2.1 min and 12.3 min appeared as the reaction time increased. The product at 2.1 min was identified as aminophenol based on its absorption characteristics. Consequently, the reduction of 4-NP to aminophenol was regarded as the key step during the photocatalytic process, which was caused by the relatively high reduction capacity of photogenerated electrons on the conduction band of $CuInS_2$. Another product at 12.3 min could be smaller molecule, and its concentration increased with prolonged irradiation and then decreased. This phenomenon indicated the intermediates were further degraded. It is worth mentioning that the photogenerated holes in $BiVO_4$ and $BiFeO_3$ could also contribute to the degradation of intermediates as
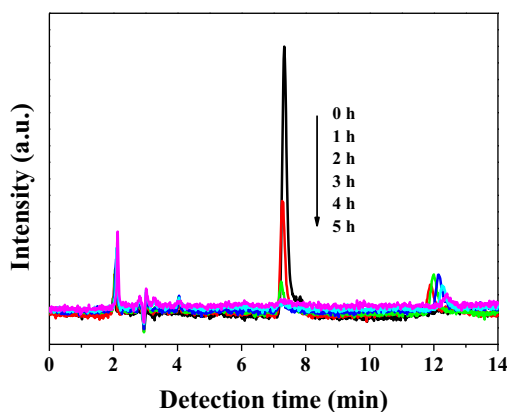
Fig. 10. HPLC spectra of 4-nitrophenol and the intermediate products during the photocatalytic process and the proposed degradation pathway (0 V vs NHE, $\lambda \geq 420$ nm).
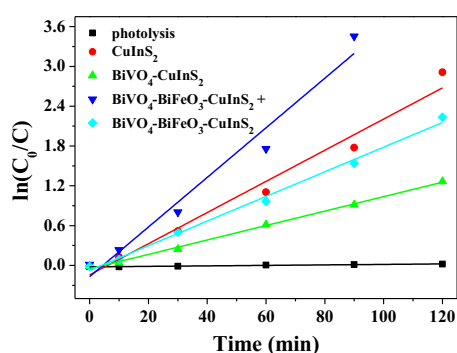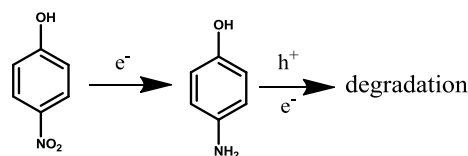

Fig. 11. Degradation kinetics of 2,4-DCP during the photocatalytic process on different photocatalysts (0 V vs NHE, $\lambda \geq 420$ nm).

they could transfer to and accumulate on the electrodes. Accordingly, the degradation process of 4-NP was proposed in Fig. 10. As the electron reduction of 4-NP was the first step during its degradation, the better performance of $BiVO_4$-$BiFeO_3$-$CuInS_2$+ was attributed to the abundant electrons on $CuInS_2$, which was supported by the results of the photocurrent density.

Chlorinated organic compounds are commonly used chemicals, for which thorough degradation is challenging due to the difficult dechlorination step. In light of the high reduction properties of $BiVO_4$-$BiFeO_3$-$CuInS_2$+, its photocatalytic performance for chlorinated organics degradation was studied using 2,4-DCP as a model pollutant. The results of the photocatalytic experiment with 2,4-DCP are shown in Figs. S7 and 11 . As can be seen, photolysis of 2,4-DCP under visible light irradiation could be neglected without photocatalysts. In accordance with the 4-NP degradation results, the highest degradation rate of 2,4-DCP was obtained in presence of $BiVO_4$-$BiFeO_3$-$CuInS_2$+, with a degradation rate constant of $2.24\,h^{-1}$. And the photocatalytic kinetic constants of 2,4-DCP degradation on $CuInS_2$ and $BiVO_4$-$CuInS_2$ were $1.41\,h^{-1}$ and $0.65\,h^{-1}$, respectively. In comparison, the photocatalytic properties of $BiVO_4$-$BiFeO_3$-$CuInS_2$ without polarization were much lower than those of $BiVO_4$-$BiFeO_3$-$CuInS_2$+, with a kinetic constant of $1.11\,h^{-1}$ on it. This result was supported by the proposed charge carrier transfer mechanism, which indicated that the poled $BiFeO_3$ layer promoted the Z-schematic charge carrier transfer between $BiVO_4$ and $CuInS_2$ and led to high redox capacity.

To explore the degradation mechanism of 2,4-DCP, the reactive active species during the photocatalytic process were studied by adding different radical scavengers, and the TOC degradation was analyzed. The results are shown in Fig. 12a and Fig. 12b, respectively. As seen in Fig. 12a, with butanol as the ·OH scavenger, the

degradation rate of 2,4-DCP remained high. This result disclosed that ·OH was not the main active species and had little effect on the degradation of 2,4-DCP over $BiVO_4$-$BiFeO_3$-$CuInS_2$+, which was due to the very tiny generation of ·OH on the photocatalysts (Fig. 6). On the contrary, h^+ and $·O_2^-$ were important active species during the pollutant degradation, as the photocatalytic rate decreased to a large extent when scavengers EDTA-2Na and *p*-benzoquinone were added to the system, respectively. Together with the result of the $·O_2^-$ generation test in Fig. 6, the active species during the photocatalytic process revealed that the superiority of $BiVO_4$-$BiFeO_3$-$CuInS_2$+ was due to the accumulation of electrons on $CuInS_2$ arising from the Z-schematic electron transfer behavior. The TOC results in Fig. 12b show very small amount of 2,4-DCP was mineralized after 2 h of 2,4-DCP degradation on $CuInS_2$ and $BiVO_4$-$CuInS_2$, even though 95% of 2,4-DCP was broken down by using $CuInS_2$ as the photocatalyst. This was caused by the weak oxidation capacity of the photogenerated holes on $CuInS_2$. In contrast, 36% TOC removal was achieved on $BiVO_4$-$BiFeO_3$-$CuInS_2$+. The much higher mineralization efficiency of 2,4-DCP was attributed to the high oxidation capacity of holes on $BiVO_4$ and the $·O_2^-$ generated during the photocatalytic process, which benefited from the Z-schematic electron transfer behavior. According to the results above, the degradation pathway of 2,4-DCP is proposed in Fig. 13.

Finally, the stability of $BiVO_4$-$BiFeO_3$-$CuInS_2$+ material was tested by the cyclic photocatalytic degradation of 2,4-DCP. During the five consecutive cycles, no significant loss of photocatalytic activity was observed for $BiVO_4$-$BiFeO_3$-$CuInS_2$+ (shown in Fig. 14a), which indicated it was stable during the photocatalytic process. Moreover, the XRD patterns of $BiVO_4$-$BiFeO_3$-$CuInS_2$+ before and after the photocatalytic degradation of 2,4-DCP were compared in Fig. 14b. It indicated that no obvious structural difference was observed for this material after its utilization, which proved it was stable during the photocatalytic reaction.

4. Conclusions

We studied, for the first time, the effect of polarization-induced electric field on the charge carrier transfer in a Z-scheme photocatalyst by inserting a poled $BiFeO_3$ layer between $BiVO_4$ and $CuInS_2$. The increased generation of reactive oxygen species and improved photocurrent density on $BiVO_4$-$BiFeO_3$-$CuInS_2$+ demonstrated that more photogenerated electrons accumulated within $CuInS_2$ in this material than in $CuInS_2$, $BiVO_4$-$CuInS_2$, and $BiVO_4$-$BiFeO_3$-$CuInS_2$. This results confirmed the polarization-induced electric field oriented from PS I to PS II (optimal thickness of 70 nm) enhanced the Z-schematic charge carrier transfer. Finally, the photocatalytic performance of $BiVO_4$-$BiFeO_3$-$CuInS_2$+ for pollutant degradation
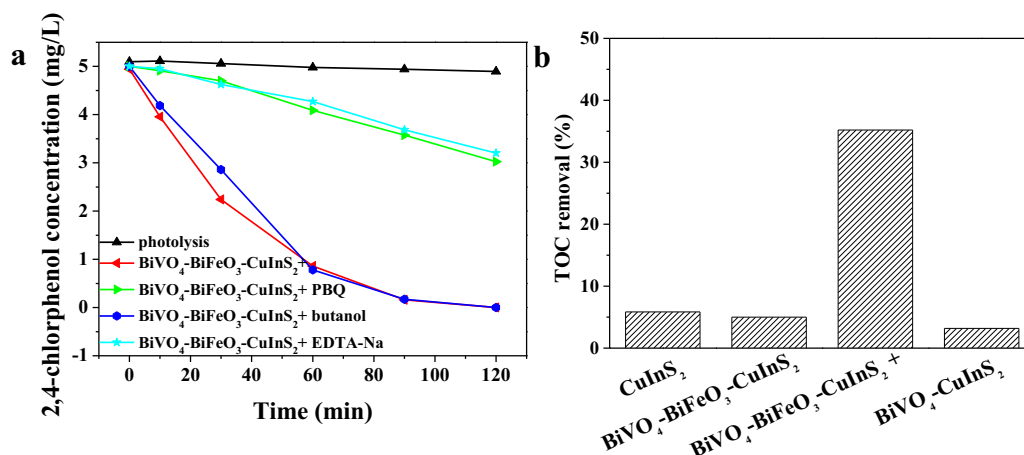
Fig. 12. (a) Concentration of 2,4-DCP versus time plots in the presence of different radical scavengers and (b) TOC variation on different photocatalysts after photocatalytic degradation of 2,4-DCP for 2 h (0 V vs NHE, $\lambda \geq 420$ nm).
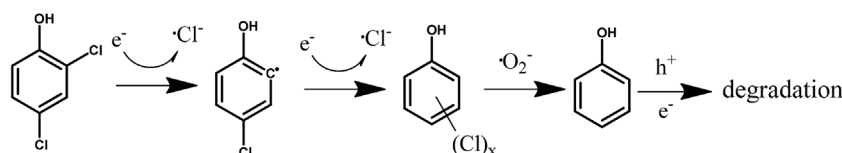

Fig. 13. Proposed degradation pathway of 2,4-DCP on $BiVO_4$-$BiFeO_3$-$CuInS_2$+ (0 V vs NHE, $\lambda \geq 420$ nm).
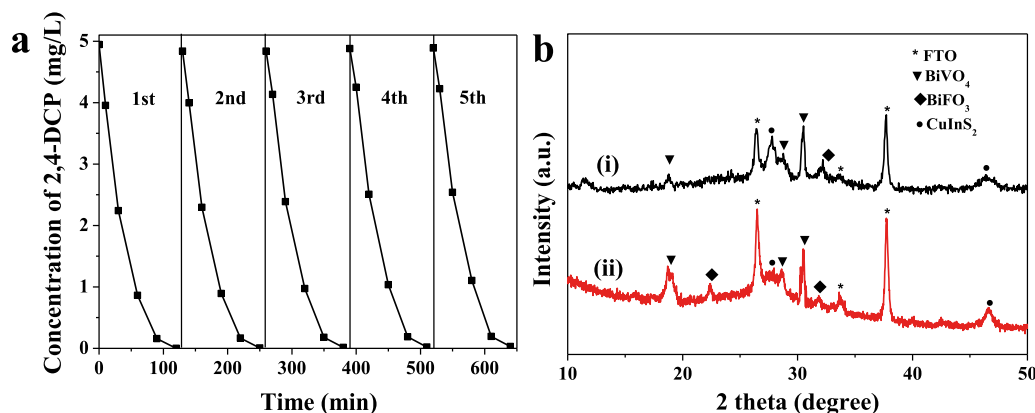

Fig. 14. (a) Cycle runs of 2,4-DCP degradation on $BiVO_4$-$BiFeO_3$-$CuInS_2$+ and (b) XRD patterns of $BiVO_4$-$BiFeO_3$-$CuInS_2$+ (i) before and (ii) after the photocatalytic process (0 V vs NHE, $\lambda \geq 420$ nm).

and mineralization was much better than those of $CuInS_2$, $BiVO_4$-$CuInS_2$, and $BiVO_4$-$BiFeO_3$-$CuInS_2$, benefiting from the Z-schematic charge carrier behavior. These findings provide a new method for the construction of Z-scheme photocatalytic systems and are important to the application of Z-scheme systems in refractory pollutant degradation.

Conflict of interest

The authors declare no competing financial interests.

Acknowledgments

Appendix A. Supplementary data

Supplementary data associated with this article can be found, in the online version, at http://dx.doi.org/10.1016/j.apcatb.2017.03.043.

Mott-Schottky plots of $BiVO_4$, $BiFeO_3$ and $CuInS_2$ (Fig. S1), energy gaps between valence bands and Fermi levels of $BiVO_4$, $BiFeO_3$, and $CuInS_2$ (Fig. S2), DRS and Tauc plots for $BiVO_4$, $BiFeO_3$ and $CuInS_2$ (Fig. S3), SEM images of $BiVO_4$, $BiFeO_3$, and $CuInS_2$ (Fig. S4), TEM images of $BiVO_4$-$BiFeO_3$-$CuInS_2$ (Fig. S5), concentration of 4-nitrophenol versus time plots (Fig. S6), and concentration of 2,4-DCP versus time plots (Fig. S7).

References

[1] M.R. Hoffmann, S.T. Martin, W.Y. Choi, D.W. Bahnemann, Environmental applications of semiconductor photocatalysis, Chem. Rev. 95 (1995) 69–96.

[2] L. Ye, J. Liu, C. Gong, L. Tian, T. Peng, L. Zan, Two different roles of metallic Ag on Ag/AgX/BiOX (X = Cl, Br) visible light photocatalysts: surface plasmon resonance and Z-scheme bridge, ACS Catal. 2 (2012) 1677–1683.

[3] A. Yella, H.W. Lee, H.N. Tsao, C.Y. Yi, A.K. Chandiran, M.K. Nazeeruddin, E.W.G. Diau, C.Y. Yeh, S.M. Zakeeruddin, M. Gratzel, Porphyrin-sensitized solar cells with cobalt (II/III)-based redox electrolyte exceed 12 percent efficiency, Science 334 (2011) 629–634.

[4] M.J. Muñoz-Batista, M.A. Nasalevich, T.J. Savenije, F. Kapteijn, J. Gascon, A. Kubacka, M. Fernández-García, Enhancing promoting effects in g-C_3N_4-M^{n+}/CeO_2-TiO_2 ternary composites: photo-handling of charge carriers, Appl. Catal. B 176–177 (2015) 687–698.

[5] K. Wang, Q. Li, B. Liu, B. Cheng, W. Ho, J. Yu, Sulfur-doped g-C_3N_4 with enhanced photocatalytic CO_2-reduction performance, Appl. Catal. B 176–177 (2015) 44–52.

[6] D. Zheng, G. zhang, X. Wang, Integrating CdS quantum dots on hollow graphitic carbon nitride nanospheres for hydrogen evolution photocatalysis, Appl. Catal. B 179 (2015) 479–488.

[7] R. Marschall, Semiconductor composites: strategies for enhancing charge carrier separation to improve photocatalytic activity, Adv. Funct. Mater. 24 (2014) 2421–2440.

[8] K. Sayama, R. Yoshida, H. Kusama, K. Okabe, Y. Abe, H. Arakawa, Photocatalytic decomposition of water into H_2 and O_2 by a two-step photoexcitation reaction using a WO_3 suspension catalyst and an Fe^{3+}/Fe^{2+} redox system, Chem. Phys. Lett. 277 (1997) 387–391.

[9] K. Sayama, K. Mukasa, R. Abe, Y. Abe, H. Arakawa, Stoichiometric water splitting into H_2 and O_2 using a mixture of two different photocatalysts and an IO_3^-/I^- shuttle redox mediator under visible light irradiation, Chem. Commun. (2001) 2416–2417.

[10] H. Tada, T. Mitsui, T. Kiyonaga, T. Akita, K. Tanaka, All-solid-state Z-scheme in CdS-Au-TiO_2 three-component nanojunction system, Nat. Mater. 5 (2006) 782–786.

[11] K.P. Xie, Q. Wu, Y.Y. Wang, W.X. Guo, M.Y. Wang, L. Sun, C.J. Lin, Electrochemical construction of Z-scheme type CdS-Ag-TiO_2 nanotube arrays with enhanced photocatalytic activity, Electrochem. Commun. 13 (2011) 1469–1472.

[12] Y. Zhou, G. Chen, Y. Yu, L. Zhao, J. Sun, F. He, H. Dong, A new oxynitride-based solid state Z-scheme photocatalytic system for efficient Cr (VI) reduction and water oxidation, Appl. Catal. B 183 (2016) 176–184.

[13] A. Kudo, Y. Miseki, Heterogeneous photocatalyst materials for water splitting, Chem. Soc. Rev. 38 (2009) 253–278.

[14] K. Maeda, Z-scheme water splitting using two different semiconductor photocatalysts, ACS Catal. 3 (2013) 1486–1503.

[15] K. Sekizawa, K. Maeda, K. Domen, K. Koike, O. Ishitani, Artificial Z-scheme constructed with a supramolecular metal complex and semiconductor for the photocatalytic reduction of CO_2, J. Am. Chem. Soc. 135 (2013) 4596–4599.

[16] J. Yan, H. Wu, H. Chen, Y. Zhang, F. Zhang, S.F. Liu, Fabrication of TiO_2/C_3N_4 heterostructure for enhanced photocatalytic Z-scheme overall water splitting, Appl. Catal. B 191 (2016) 130–137.

[17] Y. Sasaki, A. Iwase, H. Kato, A. Kudo, The effect of co-catalyst for Z-scheme photocatalysis systems with an Fe^{3+}/Fe^{2+} electron mediator on overall water splitting under visible light irradiation, J. Catal. 259 (2008) 133–137.

[18] M. Higashi, R. Abe, T. Takata, K. Domen, Photocatalytic overall water splitting under visible light using ATaO2N (A = Ca, Sr Ba) and WO3 in a IO_3^-/I^- shuttle redox mediated system, Chem. Mater. 21 (2009) 1543–1549.

[19] K. Sayama, K. Mukasa, R. Abe, Y. Abe, H. Arakawa, A new photocatalytic water splitting system under visible light irradiation mimicking a Z-scheme mechanism in photosynthesis, J. Photochem. Photobiol. A 148 (2002) 71–77.

[20] A. Iwase, Y.H. Ng, Y. Ishiguro, A. Kudo, R. Amal, Reduced graphene oxide as a solid-state electron mediator in Z-scheme photocatalytic water splitting under visible light, J. Am. Chem. Soc. 133 (2011) 11054–11057.

[21] P. Zhou, J.G. Yu, M. Jaroniec, All-solid-state Z-scheme photocatalytic systems, Adv. Mater. 26 (2014) 4920–4935.

[22] R.Q. Ye, H.B. Fang, Y.Z. Zheng, N. Li, Y. Wang, X. Tao, Fabrication of $CoTiO_3$/g-C_3N_4 hybrid photocatalysts with enhanced H_2 evolution: Z-scheme photocatalytic mechanism insight, ACS Appl. Mater. Interfaces 8 (2016) 13879–13889.

[23] Y. Sasaki, H. Nemoto, K. Saito, A. Kudo, Solar water splitting using powdered photocatalysts driven by Z-schematic interparticle electron transfer without an electron mediator, J. Phys. Chem. C 113 (2009) 17536–17542.

[24] L.L. Wang, J. Ge, A.L. Wang, M.S. Deng, X.J. Wang, S. Bai, R. Li, J. Jiang, Q. Zhang, Y. Luo, Y.J. Xiong, Designing p-type semiconductor-metal hybrid structures for improved photocatalysis, Angew. Chem. Int. Ed. 53 (2014) 5107–5111.

[25] H.F. Li, H.T. Yu, X. Quan, S. Chen, Y.B. Zhang, Uncovering the key role of the fermi level of the electron mediator in a Z-scheme photocatalyst by detecting the charge transfer process of WO_3-metal-gC_3N_4 (Metal = Cu, Ag Au), ACS Appl. Mater. Interfaces 8 (2016) 2111–2119.

[26] Z.P. Jiang, H.Y. Wang, H. Huang, C.C. Cao, Photocatalysis enhancement by electric field: TiO_2 thin film for degradation of dye X-3B, Chemosphere 56 (2004) 503–508.

[27] L. Li, P.A. Salvador, G.S. Rohrer, Photocatalysts with internal electric fields, Nanoscale 6 (2014) 24–42.

[28] M.R. Morris, S.R. Pendlebury, J. Hong, S. Dunn, J.R. Durrant, Effect of internal electric fields on charge carrier dynamics in a ferroelectric material for solar energy conversion, Adv. Mater. 28 (2016) 7123–7128.

[29] S. Dunn, D. Tiwari, Influence of ferroelectricity on the photoelectric effect of $LiNbO_3$, Appl. Phys. Lett. 93 (2008) 092905.

[30] J.W. Ager, Bucket Brigade Photovoltaic Effect in Ferroelectrics, SPIE Newsroom, 2011.

[31] Y.F. Cui, J. Briscoe, S. Dunn, Effect of ferroelectricity on solar-light-driven photocatalytic activity of $BaTiO_3$-influence on the carrier separation and stern layer formation, Chem. Mater. 25 (2013) 4215–4223.

[32] N. Hur, S. Park, P.A. Sharma, J.S. Ahn, S. Guha, S.W. Cheong, Electric polarization reversal and memory in a multiferroic material induced by magnetic fields, Nature 429 (2004) 392–395.

[33] C.H. Ahn, K.M. Rabe, J.M. Triscone, Ferroelectricity at the nanoscale: local polarization in oxide thin films and heterostructures, Science 303 (2004) 488–491.

[34] A. Iwase, S. Yoshino, T. Takayama, Y.H. Ng, R. Amal, A. Kudo, Water splitting and CO_2 reduction under visible light irradiation using Z-scheme systems consisting of metal sulfides, CoO_x-loaded $BiVO_4$, and a reduced graphene oxide electron mediator, J. Am. Chem. Soc. 138 (2016) 10260–10264.

[35] Q. Wang, T. Hisatomi, Q. Jia, H. Tokudome, M. Zhong, C. Wang, Z. Pan, T. Takata, M. Nakabayashi, N. Shibata, Y. Li, I.D. Sharp, A. Kudo, T. Yamada, K. Domen, Scalable water splitting on particulate photocatalyst sheets with a solar-to-hydrogen energy conversion efficiency exceeding 1, Nat. Mater. 15 (2016) 611–615.

[36] M. Yue, R. Wang, B. Ma, R. Cong, W. Gao, T. Yang, Superior performance of $CuInS_2$ for photocatalytic water treatment: full conversion of highly stable nitrate ions into harmless N_2 under visible light, Catal. Sci. Technol. 6 (2016) 8300–8308.

[37] Y.J. Yuan, D.Q. Chen, Y.W. Huang, Z.T. Yu, J.S. Zhong, T.T. Chen, W.G. Tu, Z.J. Guan, D.P. Cao, Z.G. Zou, MoS_2 nanosheet-modified $CuInS_2$ photocatalyst for visible-light-driven hydrogen production from water, ChemSusChem 9 (2016) 1003–1009.

[38] Y. Yu, P. Zhang, Y. Kuang, Y. Ding, J. Yao, J. Xu, Y. Cao, Adjustment and control of energy levels for TiO_2–N/$ZrO_{2-x}N_x$ with enhanced visible light photocatalytic activity, J. Phys. Chem. C 118 (2014) 20982–20988.

[39] W. Dong, Y.P. Guo, B. Guo, H. Li, H.Z. Liu, T.W. Joel, Enhanced photovoltaic effect in $BiVO_4$ semiconductor by incorporation with an ultrathin $BiFeO_3$ ferroelectric layer, ACS Appl. Mater. Interfaces 5 (2013) 6925–6929.

[40] Y. Xu, M.R. Shen, Structure and optical properties of nanocrystalline $BiFeO_3$ films prepared by chemical solution deposition, Mater. Lett. 62 (2008) 3600–3602.

[41] M.X. Zhuang, A.X. Wei, Y. Zhao, J. Liu, Z.Q. Yan, Z. Liu, Morphology-controlled growth of special nanostructure $CuInS_2$ thin films on an FTO substrate and their application in thin film solar cells, Int. J. Hydrogen Energy 40 (2015) 806–814.

[42] W.G. Yang, Y.H. Yu, M.B. Starr, X. Yin, Z.D. Li, A. Kvit, S.F. Wang, P. Zhao, X.D. Wang, Ferroelectric polarization-enhanced photoelectrochemical water splitting in TiO_2-$BaTiO_3$ core-shell nanowire photoanodes, Nano Lett. 15 (2015) 7574–7580.

[43] A.J. Bard, R. Parsons, J. Jordan, Standard Potentials in Aqueous Solution, Marcel Dekker, New York, 1985.

[44] J.L. Wang, Y. Yu, L.Z. Zhang, Highly efficient photocatalytic removal of sodium pentachlorophenate with Bi_3O_4Br under visible light, Appl. Catal. B 136 (2013) 112–121.

[45] I. Saito, M. Takayama, T. Matsuura, S. Matsugo, S. Kawanishi, Phthalimide hydroperoxides as efficient photochemical hydroxyl radical generators – a novel DNA-cleaving agent, J. Am. Chem. Soc. 112 (1990) 883–884.

[46] V. Brezova, S. Gabcova, D. Dvoranova, A. Stasko, Reactive oxygen species produced upon photoexcitation of sunscreens containing titanium dioxide (an EPR study), J. Photochem. Photobiol. B 79 (2005) 121–134.